



# An Implementation of Galactic White Dwarf Binary Data Analysis for MLDC-3.1

Yang Lu (卢杨) , En-Kun Li (李恩坤) <sup>1</sup>, Yi-Ming Hu (胡一鸣) <sup>1</sup>, Jian-dong Zhang (张建东) , and Jianwei Mei (梅健伟)  
 MOE Key Laboratory of TianQin Mission, TianQin Research Center for Gravitational Physics & School of Physics and Astronomy, Frontiers Science Center for  
 TianQin, Gravitational Wave Research Center of CNSA, Sun Yat-sen University (Zhuhai Campus), Zhuhai 519082, China; [lienk@mail.sysu.edu.cn](mailto:lienk@mail.sysu.edu.cn),  
[huyiming@mail.sysu.edu.cn](mailto:huyiming@mail.sysu.edu.cn), [zhangjd9@mail.sysu.edu.cn](mailto:zhangjd9@mail.sysu.edu.cn), [meijw@mail.sysu.edu.cn](mailto:meijw@mail.sysu.edu.cn)

Received 2022 October 3; revised 2022 November 5; accepted 2022 November 29; published 2023 January 11

## Abstract

The space-borne gravitational wave detectors will observe a large population of double white dwarf binaries in the Milky Way. However, the search for double white dwarfs in the gravitational wave data will be time-consuming due to the large number of templates involved and antenna response calculation. In this paper, we implement an iterative combinatorial algorithm to search for double white dwarfs in MLDC-3.1 data. To quickly determine the rough parameters of the target sources, the following algorithms are adopted in a coarse search process: (1) using the downsampling method to reduce the number of original data points; (2) using the undersampling method to speed up the generation of a single waveform template; (3) using the stochastic template bank method to quickly construct the waveform template bank while achieving high coverage of the parameter space; (4) combining the FFT acceleration algorithm with the stochastic template bank to reduce the calculation time of a single template. A fine search process is applied to further determine the parameters of the signals based on the coarse search, for which we adopt the particle swarm optimization. Finally, we detect  $\mathcal{O}(10^4)$  double white dwarf signals, validating the feasibility of our method.

**Key words:** (stars:) white dwarfs – (stars:) binaries: general – gravitational waves

## 1. Introduction

The first observation of a gravitational wave (GW) signal, i.e., GW150914, was made by Advanced LIGO (Abbott et al. 2016), marking the beginning of a new era in observing the universe with GW. So far, 90 compact binary mergers have been reported by the LIGO-Virgo-KAGRA collaborations (Abbott et al. 2019, 2021a, 2021b, 2021c). With the lower frequency cut-off determined by the Earth's large seismic and gravity-gradient noises (Accadia et al. 2012; Aso et al. 2013; Hall et al. 2019), ground-based GW detectors, such as Advanced LIGO (Aasi et al. 2015), Advanced Virgo (Acernese et al. 2015) and KAGRA (Somiya 2012), are operated in the  $10\text{--}10^3$  Hz frequency band. However, there are a large number of GW sources in the millihertz (mHz) band, such as massive black hole binaries (Wang et al. 2019; Katz et al. 2020), extreme mass ratio inspirals (Calabrese et al. 2017; Fan et al. 2020), stellar-mass binary black holes (Kyutoku & Seto 2016; Sesana 2016; Liu et al. 2020), double white dwarfs (DWDs) (Nelemans et al. 2001a; Yu & Jeffery 2010; Breivik et al. 2020; Huang et al. 2020) and stochastic backgrounds of astrophysical and cosmological origin (Romano & Cornish 2017; Liang et al. 2021). All these sources can be detected by the proposed space-

borne GW detectors, e.g., TianQin (Luo et al. 2016) and LISA (Amaro-Seoane et al. 2017).

In the mHz frequency range, binary star systems are mainly composed of DWD binaries in the Milky Way ( $\mathcal{O}(10^8)$ ) (Nelemans et al. 2001a). Due to their large number, DWDs are expected to be the most numerous GW sources for space-borne detectors, and about ten thousand DWD binaries will be detected by LISA and TianQin (Nelemans et al. 2001a; Yu & Jeffery 2010; Lamberts et al. 2018; Breivik et al. 2020; Huang et al. 2020). The detection of GWs from DWDs will significantly improve our understanding of stellar evolution, Galactic compact binary systems, the distribution of stars in the Milky Way, etc. More specifically, (1) DWD mergers are one of the main candidate mechanisms for type Ia supernova explosions. In addition, the near-infrared magnitudes of type Ia supernovae are considered to be the best “standard candles” (Barone-Nugent et al. 2012), which are of great importance for the study of modern cosmology (Riess et al. 1998; Perlmutter et al. 1999). (2) DWDs are the end products of the evolution of stellar binaries, so the detection of GWs from DWDs can shed light on the formation and evolution of stellar binaries (Belczynski et al. 2001; Postnov & Yungelson 2014). (3) Due to the mass-transfer, DWDs can form AM Canum Venaticorum (AM CVn) systems, thus, using GW observations in combination with electromagnetic observations can probe the physics of mass transfer processes (Nelemans et al. 2001b; Marsh et al.

<sup>1</sup> Corresponding authors.

2004; Solheim 2010; Tauris 2018). (4) The detached DWDs with short orbital periods (ranging from one hour to a few minutes) are particularly suitable in studying the physics of tides (Fuller & Lai 2012; Dall’Osso & Rossi 2014). (5) The overall GW signals from DWDs imprint information about the entire Galaxy’s stellar population, which is helpful in figuring out the structural properties of the Milky Way (Benacquista & Holley-Bockelmann 2006; Adams et al. 2012; Korol et al. 2019; Breivik et al. 2020; Wilhelm et al. 2020).

Although the huge amount of DWDs could bring us a wealth of information on GWs, its detection also poses great challenges. First, the superposition of GW signals from DWDs can form a confusion noise in space-borne detectors (Timpano et al. 2006; Huang et al. 2020; Liang et al. 2021). That means the received DWD signals can be confused with each other to the point where individual binaries cannot be resolved (Crowder & Cornish 2004). Second, about ten thousand DWDs will be resolvable due to either their isolation in frequency space or their relative brightness, and how to effectively detect these DWD signals has become a big challenge (Timpano et al. 2006; Yu & Jeffery 2010; Lamberts et al. 2018; Breivik et al. 2020; Huang et al. 2020).

To solve this problem and develop LISA data analysis algorithms, LISA organized four rounds of mock data challenges from 2006 to 2010, called Mock LISA Data Challenge (MLDC) (Arnaud et al. 2006, 2007a, 2007b; MLDC 2006; Babak et al. 2008a, 2008b, 2010). Since 2019, LISA has started a new round of data challenges, named LISA Data Challenges (LDC) (LDC 2019). The amount of DWD signals contained in different rounds of MLDC varies enormously, e.g., MLDC-1.1 consists of three single source data sets and four multiple source data sets (Arnaud et al. 2007b); MLDC-2.1 contains about 26 million DWD signals (Arnaud et al. 2007a); MLDC-3.1 has about 60 million DWD signals (Babak et al. 2008b); MLDC-4 is the “whole enchilada challenge,” which includes all the sources of MLDC 3.1-3.5 in one data set (Babak et al. 2010).

The majority of methods utilized to detect the DWD signals in MLDC data set are based on the matched filtering technique, which calculates the correlation between the data and the expected waveform, and is an optimal strategy in detecting signals in additive, Gaussian, stationary noise (Helström 1968). Depending on whether a pre-set bank of templates is required, the detection methods can be divided into two categories: stochastic search and grid-based search (Blaut et al. 2010).

For the stochastic search, no template is used for the signal search, and a typical implementation involves the Markov Chain Monte Carlo (MCMC) algorithm. Applying an F-MCMC algorithm, (Cornish & Crowder 2005) resulted in correctly identifying the number and source parameters of GW signals from multiple Galactic binaries within simulated LISA data streams. Using an extension of the MCMC method named blocked-annealed Metropolis-Hastings (BAM) proposed in

Crowder & Cornish (2007), Littenberg (2011) reported about 9000 sources in MLDC-4 data. Applying a Metropolis-Hastings Monte Carlo (MHMC) code, the Montana State-JPL (MTJPL) collaboration reported 19,324 sources<sup>2</sup> in the MLDC-2.1 data set (Babak et al. 2008a). Adopting the particle swarm optimization (PSO) algorithm with the rejection of spurious sources by cross-validating, Zhang et al. (2021) reported 12,270 sources in LDC 1-4 and 12,044 sources in MLDC-3.1mod<sup>3</sup>.

Different from a stochastic search, which concentrates on the regions with high likelihood (Blaut et al. 2010), a grid-based search maps the whole parameter space by constructing grids in parameter space. Constructing a template bank in the parameter space needs to balance a number of conflicting constraints: too dense templates will waste computing resources, and too loose templates will easily miss signals. Template-based searches for GWs are often limited by the computational cost associated with searching a large parameter space. So, it is important to study how to place templates effectively and concisely in the parameter space (John & Neil Sloane 1999; Prix 2007). The problem of constructing a grid is equivalent to the problem of covering  $d$ -dimensional space with identical hyperellipsoids or overlapping regular lattices (John & Neil Sloane 1999). For example, the hypercubic  $\mathbb{Z}_n$  lattice and the  $A_n^*$  lattice (John Conway & Neil Sloane 1999; Messenger et al. 2009) are used to construct an efficient template bank, which was widely implement in searching for continuous GWs by LIGO (Babak et al. 2006; Astone et al. 2010; Allen et al. 2012; Wette 2014; Pisarski & Jaranowski 2015) and LISA (Brown et al. 2007; Blaut et al. 2009). Using reduced Fisher matrices to build the template grid, Blaut et al. (2010) reported 12,805 sources in MLDC-3.1 data. Another more convenient method to place templates is random or stochastic methods<sup>4</sup>, which are more effective in high-dimensional parameter space and if the parameter space metric<sup>5</sup> is non-flat (Babak 2008; Harry et al. 2009; Messenger et al. 2009; Fehrmann & Pletsch 2014; Allen 2022). To make the template coverage more effective, numerous algorithms had been applied to prune the random template bank, e.g., remove those which are “too close” together, adjust their positions, etc. (Harry et al. 2009; Manca & Vallisneri 2010; Fehrmann & Pletsch 2014). Throughout the manuscript we call such method a “stochastic template bank”.

In this paper, we implement an iterative source subtraction method to detect DWDs. For quick searches of all the expected candidate signals injected in the “observation” data set, the

<sup>2</sup> <http://www.tapir.caltech.edu/~mldc/results2/MTJPL-writeup-070618-161814.pdf>

<sup>3</sup> The authors add the GW signals used in MLDC-3.1 to the noise realizations in LDC 1-4.

<sup>4</sup> The largest difference between random and stochastic methods is whether there are any additional pruning steps.

<sup>5</sup> The metric is defined as a distance measure, which is related to the loss in matched filter SNR for a given template and signal (Messenger et al. 2009).

following methods will be adopted to speed up the calculation: (1) the downsampling method is applied to reduce data points (Błaut et al. 2010); (2) the undersampling method is utilized to speed up the generation of waveforms in the template bank (Zhang et al. 2021); (3) the “Fast Fourier Transform (FFT)” algorithm is used to reduce the calculation time of each detection statistic (Jaranowski & Krolak 2005; Błaut et al. 2010); (4) stochastic template bank method is implemented to improve the coverage of parameter space. We call this process *coarse search*. Some simplifications are removed in the *fine search* procedure so that the parameters are more precisely recovered. Based on the candidates provided by the coarse search, we use the PSO algorithm to explore the parameter space.

The paper is organized as follows. A brief review of relevant background information is presented in Section 2. The method of downsampling the original data and method of generating waveforms with undersampling are introduced in Section 3. Details about the search method and pipeline are discussed in Section 4. Section 5 is the search results and discussions. Section 6 is the conclusion.

## 2. Background

### 2.1. GW Signal of DWD

In the mHz frequency band, the DWDs are expected to exhibit relatively little frequency evolution. Thus, the GW strain emitted from a DWD can be safely approximated as (in the source frame)

$$h_+(t) = A_+ \cos \Phi(t) = h_0 \frac{1 + \cos^2 \iota}{2} \cos \Phi(t), \quad (1)$$

$$h_\times(t) = A_\times \sin \Phi(t) = h_0 \cos \iota \sin \Phi(t), \quad (2)$$

$$h_0 = \frac{4(G\mathcal{M}_c)^{5/3}}{c^4 D_L} (\pi f)^{2/3}, \quad (3)$$

$$\Phi(t) = 2\pi f t + \pi \dot{f} t^2 + \phi_0, \quad (4)$$

where  $+$ ,  $\times$  represent the two polarization modes of GWs,  $\iota$  is the inclination angle of the quadruple rotation axis with respect to the line of sight (the direction is from the source to the Sun),  $\mathcal{M}_c = (m_1 m_2)^{3/5} / (m_1 + m_2)^{1/5}$  ( $m_1$  and  $m_2$  are the individual masses of the components of the binary) is the chirp mass of the system,  $D_L$  is the luminosity distance to the source,  $\phi_0$  is the initial phase at the start of the observation,  $f$  and  $\dot{f}$  are the frequency of the source and its derivative with respect to time respectively, and  $G$  and  $c$  are the gravitational constant and speed of light respectively.

Considering the motion of the detectors moving around the Sun, a Doppler modulation of the phase of the waveform should be taken into account, i.e.,

$$\Phi(t) \rightarrow \Phi(t) + \Phi_D(t), \quad (5)$$

$$\Phi_D(t) = 2\pi(f + \dot{f}t) \frac{R}{c} \cos \beta \cos(2\pi f_m t - \lambda), \quad (6)$$

where  $\Phi_D(t)$  is the Doppler modulation,  $f_m = 1 \text{ yr}$  is the modulation frequency,  $\beta$  and  $\lambda$  are the latitude and longitude of the source in ecliptic coordinates respectively, and  $R = 1 \text{ au}$  is the semimajor axis of the guiding center of the satellite constellation.

The measured scalar GW signal at time  $t$  by detector channel  $\mathcal{I}$  is denoted as  $h^\mathcal{I}(t)$ . It is the response of the detector to the GW tensor

$$h^\mathcal{I}(t) = \sum_{a=+, \times} F^{a,\mathcal{I}}(t; \lambda, \beta, \psi) h_a(t; f, \dot{f}, h_0, \iota, \phi_0), \quad (7)$$

where  $F^{a,\mathcal{I}}$  is antenna pattern functions of detector channel  $\mathcal{I}$ , and  $\psi$  is the polarization angle that describes the wave frame with respect to the equatorial coordinate system.

In the present paper, we will use the  $\mathcal{F}$ -statistic method (Jaranowski et al. 1998) for signal detection, with which the measured signal can be decomposed into time-dependent and time-independent parts

$$h^\mathcal{I}(t) = \sum_{\mu=1}^4 \mathcal{A}^\mu(h_0, \iota, \phi_0, \psi) h_\mu^\mathcal{I}(t; f, \dot{f}, \lambda, \beta), \quad (8)$$

where  $\mathcal{A}^\mu$  is the signal-amplitudes, which depend only on the four *extrinsic parameters*  $\{h_0, \iota, \phi_0, \psi\}$ , and are independent of the detector  $\mathcal{I}$ ,

$$\begin{aligned} \mathcal{A}^1 &= A_+ \cos \phi_0 \cos 2\psi - A_\times \sin \phi_0 \sin 2\psi, \\ \mathcal{A}^2 &= A_+ \cos \phi_0 \sin 2\psi + A_\times \sin \phi_0 \cos 2\psi, \\ \mathcal{A}^3 &= -A_+ \sin \phi_0 \cos 2\psi - A_\times \cos \phi_0 \sin 2\psi, \\ \mathcal{A}^4 &= -A_+ \sin \phi_0 \sin 2\psi + A_\times \cos \phi_0 \cos 2\psi. \end{aligned} \quad (9)$$

The four basis waveforms  $h_\mu^\mathcal{I}$ , which depend only on the four *intrinsic parameters*  $\Theta = \{f, \dot{f}, \lambda, \beta\}$ , are related to the specifics of the detectors and can be written as<sup>6</sup>

$$\begin{aligned} h_1^\mathcal{I}(t) &= a^\mathcal{I}(t) \cos \phi^\mathcal{I}(t), & h_2^\mathcal{I}(t) &= b^\mathcal{I}(t) \cos \phi^\mathcal{I}(t), \\ h_3^\mathcal{I}(t) &= a^\mathcal{I}(t) \sin \phi^\mathcal{I}(t), & h_4^\mathcal{I}(t) &= b^\mathcal{I}(t) \sin \phi^\mathcal{I}(t), \end{aligned} \quad (10)$$

where  $a^\mathcal{I}(t)$  and  $b^\mathcal{I}(t)$  are the antenna-pattern functions, which depend on the sky position of the DWDs and the features of the detector, and  $\phi^\mathcal{I}(t) = \Phi(t) - \phi_0$  is the signal phase at the detector channel  $\mathcal{I}$ .

### 2.2. The Noise Model

We will focus on the case when the instrumental noise  $n(t)$  is assumed to be Gaussian stationary with a zero mean. Thus, the ensemble average of the Fourier components of the noise  $n(f)$

<sup>6</sup> Note that we have suppressed the parameters except for  $t$ .

can be written in the following form

$$\langle \tilde{n}(f) \tilde{n}^*(f') \rangle = \frac{1}{2} \delta(f - f') S_n(f), \quad (11)$$

where  $*$  denotes complex conjugate, and  $S_n(f)$  is the single-sided noise power spectral density (PSD).<sup>7</sup>

Space-borne GW detection suffers from laser phase noise, which can be alleviated through Time-Delay Interferometry (TDI) technology. TDI essentially constructs virtually equal-arm interferometers so that the laser phase noise cancels out exactly. The three symmetric Michelson channels for each interferometer after TDI are named channels  $X$ ,  $Y$  and  $Z$ , and the MLDC data are expressed in such form (Armstrong et al. 1999; Krolak et al. 2004). However, different channels will use the same link, then the instrumental noises in different channels may be correlated with each other. Considering that all the satellites are identical, we can get one “optimal” combination by linear combinations of  $X$ ,  $Y$  and  $Z$  (Prince et al. 2002)

$$\begin{aligned} A &= \frac{Z - X}{\sqrt{2}}, \\ E &= \frac{X - 2Y + Z}{\sqrt{6}}, \\ T &= \frac{X + Y + Z}{\sqrt{3}}. \end{aligned} \quad (12)$$

In the  $A$ ,  $E$  and  $T$  channels, the instrumental noise is orthogonal, and consequently, the noise correlation matrix of these three combinations is diagonal (Prince et al. 2002). Thus, in the present paper, if there are no special instructions, the detector channel  $\mathcal{I}$  will iterate through  $A$ ,  $E$ , or  $T$ . The details of  $h_\mu^{A,E,T}(t)$  can be found in Błaut et al. (2010).

For a space-borne GW detector with three satellites forming an approximately equilateral triangle, the PSDs of noise for the TDI  $A$ ,  $E$  and  $T$  channels are (Estabrook et al. 2000; Błaut et al. 2010):

$$\begin{aligned} S_n^A(f) &= S_n^E(f) \\ &= 32 \cos(\omega L/2)^2 \sin(\omega L/2)^2 \\ &\quad \times \{ [6 + 4 \cos(\omega L) + 2 \cos(2\omega L)] S^{\text{acc}} \\ &\quad + [2 + \cos(\omega L)] S^{\text{opt}} \}, \\ S_n^T(f) &= 128 \cos(\omega L/2)^2 \sin(\omega L/2)^4 \\ &\quad \times [4 \sin(\omega L/2)^2 S^{\text{acc}} + S^{\text{opt}}], \end{aligned} \quad (13)$$

where  $\omega = 2\pi f$  is the angular frequency,  $L$  is the arm-length between the satellites,  $S^{\text{acc}}$  is the PSD of the proof-mass noises and  $S^{\text{opt}}$  is the PSD of the optical-path noises (Babak et al. 2008b) (the parameters used in this article can be found in Appendix A).

Apart from the instrumental noises, the waveforms of a large number of DWD signals may overlap to create a confusion

foreground. One of the most challenging tasks for the DWD search is to identify individual signals from the foreground. The unresolved binary systems can form a non-stationary confusion noise that should be added to the overall noise level of space-borne detectors (Timpano et al. 2006). In the process of our analysis, we have included the PSD of the foreground noise, see Appendix B for more details.

### 2.3. Likelihood Function

Since the true parameters of a GW signal in the time series data  $x(t)^{\mathcal{I}}$  are unknown, one can use a waveform  $h(t)^{\mathcal{I}}$  which closely mimics the signal, and the residuals  $n^{\mathcal{I}}(t) = x^{\mathcal{I}}(t) - h^{\mathcal{I}}(t)$  should be consistent with our model of the instrumental noise. In the case of stationary Gaussian noise,  $n^{\mathcal{I}}(t) \sim \mathcal{N}(0, S_n^{\mathcal{I}})$ . Then, the likelihood function with only noise in data can be written as (Finn 1992; Cutler & Schutz 2005; Prix 2007; Allen et al. 2012; Babak et al. 2010)

$$P(n^{\mathcal{I}}(t) | S_n^{\mathcal{I}}) = \kappa \exp \left[ -\frac{1}{2} (n^{\mathcal{I}}(t) | n^{\mathcal{I}}(t)) \right], \quad (14)$$

where  $\kappa$  is the normalization constant, and the inner product  $(\cdot | \cdot)$  is the scalar product which is defined as (Finn 1992; Cutler & Flanagan 1994)

$$(x(t) | y(t)) \equiv 4 \text{Re} \int_0^{+\infty} \frac{\tilde{x}(f) \tilde{y}^*(f)}{S_n(f)} df, \quad (15)$$

where  $\tilde{x}(f)$  is the Fourier transform (FT) of  $x(t)$ .

Using Equation (14), the likelihood of observing data  $x^{\mathcal{I}}(t)$  with a signal  $h^{\mathcal{I}}(t)$  should be expressed as

$$P(x^{\mathcal{I}} | h^{\mathcal{I}}, S_n^{\mathcal{I}}) = \kappa \exp \left[ -\frac{1}{2} (x^{\mathcal{I}} - h^{\mathcal{I}} | x^{\mathcal{I}} - h^{\mathcal{I}}) \right]. \quad (16)$$

Combining Equations (14) and (16), and to put information from all channels into calculation, the optimal detection statistic can be given by the likelihood ratio

$$\begin{aligned} \log \Lambda &= \log \prod_{\mathcal{I}} \frac{P(x^{\mathcal{I}}(t) | h^{\mathcal{I}}(t), S_n^{\mathcal{I}})}{P(n^{\mathcal{I}}(t) | S_n^{\mathcal{I}})} \\ &= \sum_{\mathcal{I}} \left( (x^{\mathcal{I}}(t) | h^{\mathcal{I}}(t)) - \frac{1}{2} (h^{\mathcal{I}}(t) | h^{\mathcal{I}}(t)) \right), \end{aligned} \quad (17)$$

where the product/summation implies the assumption that the noises between different channels are independent.

The GW signal produced by the DWD is approximately a monochromatic source. Thus, over the narrow bandwidth of the signal, we assume the spectral density of the noise can be approximated by a constant, i.e.,  $S_n(f) \approx S_n(f_0)$ , where  $f_0$  will be some “central” frequency of the bandwidth or the frequency of the signal (Błaut et al. 2010; Pisarski & Jaranowski 2015). Employing Parseval’s theorem, Equation (15) can be

<sup>7</sup> This is due to the fact that  $n(t)$  is real,  $\tilde{n}^*(f) = \tilde{n}(-f)$  and therefore  $S_n(-f) = S_n(f)$ .



approximated by Astone et al. (2010)

$$(x(t)|y(t)) \approx \frac{2}{S_n(f_0)} \int_0^{T_0} x(t)y(t)dt, \quad (18)$$

where  $T_0$  is the observation time, and  $x^{\mathcal{I}}(t)$  and  $y^{\mathcal{I}}(t)$  are some narrowband continuous wave signals at frequency  $f_0$  or the measured data in the narrow bandwidth around  $f_0$ .

Using Equation (18) the log likelihood ratio in Equation (17) can be written as

$$\log \Lambda = \sum_{\mathcal{I}} \frac{2T_0}{S_n^{\mathcal{I}}(f_0)} \left( \langle x^{\mathcal{I}}(t)h^{\mathcal{I}}(t) \rangle - \frac{1}{2} \langle h^{\mathcal{I}}(t)h^{\mathcal{I}}(t) \rangle \right). \quad (19)$$

Due to the stationarity of the noise, here we replace the ensemble average defined in Equation (11) with time average (Astone et al. 2010; Błaut et al. 2010)

$$\langle x(t) \rangle = \frac{1}{T_0} \int_0^{T_0} x(t)dt. \quad (20)$$

#### 2.4. $\mathcal{F}$ -statistic

The  $\mathcal{F}$ -statistic method is a matched-filtering detection statistic for continuous GWs, which was first introduced by Jaranowski et al. (1998), and subsequently generalized to the multidetector case (Krolak et al. 2004; Cornish & Crowder 2005; Cutler & Schutz 2005). In the analysis of continuous GWs, adopting this method can reduce the parameter space to include only the parameters affecting the time evolution of the signal phase (Jaranowski et al. 1998; Prix 2007). This method has been widely utilized in continuous GW searches, e.g., searches for continuous GWs from spinning neutron stars (Abbott et al. 2004, 2007) and DWD signals in MLDC (Babak et al. 2008a, 2008b, 2010).

Assuming there is only one signal contained in the data, then the parameters of a DWD signal can be estimated using the maximum likelihood estimation method. Combining Equation (8), the log likelihood ratio in Equation (19) can be rewritten as

$$\log \Lambda = \frac{2T_0}{S_n^{\mathcal{I}}(f_0)} \sum_{\mathcal{I}} \left( \mathcal{A}^{\mu} x_{\mu}^{\mathcal{I}} - \frac{1}{2} \mathcal{A}^{\mu} \mathcal{M}_{\mu\nu} \mathcal{A}^{\nu} \right), \quad (21)$$

where the Einstein summation convention is adopted for Greek indices,  $\mu, \nu \in [1, 4]$  and

$$\begin{aligned} x_{\mu}^{\mathcal{I}} &= \sum_{\mathcal{I}} \langle x^{\mathcal{I}}(t) h_{\mu}^{\mathcal{I}}(t, \Theta) \rangle, \\ \mathcal{M}_{\mu\nu} &= \sum_{\mathcal{I}} \langle h_{\mu}^{\mathcal{I}}(t, \Theta) h_{\nu}^{\mathcal{I}}(t, \Theta) \rangle. \end{aligned} \quad (22)$$

Analytically utilizing the maximum log likelihood ratio (MLR) over  $\mathcal{A}^{\mu}$  yields the so called  $\mathcal{F}$ -statistic (Jaranowski et al. 1998)

$$\mathcal{F} \equiv \max_{\mathcal{A}} \log \Lambda = \frac{T_0}{S_n^{\mathcal{I}}(f_0)} \sum_{\mathcal{I}} x_{\mu}^{\mathcal{I}} \mathcal{M}^{\mu\nu} x_{\nu}^{\mathcal{I}}, \quad (23)$$

where  $\mathcal{M}^{\mu\nu}$  is the inverse of  $\mathcal{M}_{\mu\nu}$ , i.e.,  $\mathcal{M}_{\mu\alpha} \mathcal{M}^{\alpha\nu} = \delta_{\mu}^{\nu}$ . Moreover under the MLR condition, the estimator of  $\mathcal{A}_{\text{MLR}}^{\mu}$  is

$$\mathcal{A}_{\text{MLR}}^{\mu} = \sum_{\mathcal{I}} \mathcal{M}^{\mu\nu} x_{\nu}^{\mathcal{I}}. \quad (24)$$

According to Equation (9), once the four values of  $\mathcal{A}^{\mu}$  are determined, the values of  $\{h_0, \iota, \phi_0, \psi\}$  can be obtained analytically (see Appendix C).

When the target intrinsic parameters are perfectly matched to the signal, the expectation of the  $\mathcal{F}$ -statistic (in Equation (23)) is (Cutler & Schutz 2005; Prix 2007)

$$E[2\mathcal{F}] = 4 + \rho^2, \quad (25)$$

where  $\rho$  is optimal signal-to-noise ratio (SNR), and  $\rho^2 = \sum_{\mathcal{I}} \langle h^{\mathcal{I}} | h^{\mathcal{I}} \rangle$ .

#### 2.5. Acceleration algorithm

According to Błaut et al. (2010) for a grid-based search, the FFT algorithm can be used to speed up calculation of the  $\mathcal{F}$ -statistic in detecting GW signals from DWDs in the MLDC data set (Błaut et al. 2010). Just as in Błaut et al. (2010), combining with Equation (22), after some mathematical manipulation, Equation (23) can be rewritten in a more compact form of expression

$$\begin{aligned} \mathcal{F} &= 2 \frac{T_0}{S_n^{\mathcal{I}}(f_0)} \sum_{\mathcal{I}} \\ &\times \frac{\{V | N^{(u)} |^2 + U | N^{(v)} |^2 - 2 \operatorname{Re}[W N^{(u)} (N^{(v)})^*]\}}{UV - |W|^2}, \end{aligned} \quad (26)$$

where

$$\begin{aligned} U &= 2 \langle h_1^{\mathcal{I}}(t, \Theta) h_1^{\mathcal{I}}(t, \Theta) \rangle, \\ V &= 2 \langle h_2^{\mathcal{I}}(t, \Theta) h_2^{\mathcal{I}}(t, \Theta) \rangle, Q = 2 \langle h_1^{\mathcal{I}}(t, \Theta) h_2^{\mathcal{I}}(t, \Theta) \rangle, \\ P &= 2 \langle h_1^{\mathcal{I}}(t, \Theta) h_4^{\mathcal{I}}(t, \Theta) \rangle, \end{aligned} \quad (27)$$

are some components of the matrix  $\mathcal{M}_{\mu\nu}$  defined in Equation (22),  $W = Q + iP$  and

$$\begin{aligned} N^{(u)} &= x_1^{\mathcal{I}} + ix_3^{\mathcal{I}} \\ &= 4\pi f L \sin(2\pi f L) \langle x^{\mathcal{I}}(t) m^{(u)}(t) \exp(i\phi^{\mathcal{I}}(t)) \rangle, \\ N^{(v)} &= x_2^{\mathcal{I}} + ix_4^{\mathcal{I}} \\ &= 4\pi f L \sin(2\pi f L) \langle x^{\mathcal{I}}(t) m^{(v)}(t) \exp(i\phi^{\mathcal{I}}(t)) \rangle, \end{aligned} \quad (28)$$

where  $m^{(u)}$  and  $m^{(v)}$  are complex modulation functions as defined in Błaut et al. (2010). Splitting  $\phi(t)$  as  $2\pi f t + \phi_{\text{mod}}$ , where  $\phi_{\text{mod}} = \pi \dot{f} t^2 + \Phi_D(t)$ , from Equation (26) one can get a general integral part

$$\begin{aligned} I^{\mathcal{I}} &= \int_0^{T_0} x^{\mathcal{I}}(t) m(t; f, \beta, \lambda) \\ &\exp[i\phi_{\text{mod}}(t; f, \dot{f}, \beta, \lambda)] \times \exp[i2\pi f t] dt. \end{aligned} \quad (29)$$

This integral will be an FT if both the phase modulation function  $\phi_{\text{mod}}$  and the complex modulation function  $m$  are independent of the frequency  $f$ .

In a narrow frequency band, e.g., 0.1 mHz,  $\phi_{\text{mod}}$  and  $m$  can be assumed to be constant and approximately represented with the value at the middle frequency of the band, i.e.,  $f_c$ . Consequently, the integral of Equation (29) can be approximated by

$$I^{\mathcal{I}} \simeq \int_0^{T_0} x^{\mathcal{I}}(t) m(t; f_c, \beta, \lambda) \exp[i\phi_{\text{mod}}(t; f_c, \dot{f}, \beta, \lambda)] \times \exp[i2\pi f t] dt. \quad (30)$$

Thus, one can construct the template bank with the nodes of the grid coinciding with the Fourier frequencies, which allows us to compute the  $\mathcal{F}$ -statistic using the FFT algorithm.

### 3. Preparing the Data and GW Template

The challenge data set MLDC-3.1 (Prix & Whelan 2007) in which about  $6 \times 10^7$  Galactic binaries are buried is used as the target data set in the present paper. Among all the signals,  $\sim 2.61 \times 10^7$  are detached, which mean that the two components are clearly delineated, separated stars, and  $\sim 3.42 \times 10^7$  are interacting Galactic binaries, which mean that the two components interact in that there is a mass transfer. The data set contains a two year long data set ( $2^{22}$  samples with 15 s sampling) with the first generation of TDI observables  $X$ ,  $Y$  and  $Z$ . We aim to detect as many as possible of the DWD GW signals from the 40,628 “bright” signals.<sup>8</sup>

A given DWD system will rotate through a large number of cycles during the two year period. This translates to a very small volume in parameter space that any template can cover. Combined with a large number of target sources, the computational burden can be extraordinary. In this section, we introduce tricks like downsampling and undersampling, which can decrease the total search time by roughly two orders of magnitude.

#### 3.1. Downsampling

A large number of data points is a big challenge to the calculation. In order to improve the efficiency of calculation, we first apply downsampling to the data (Blaut et al. 2010). Downsampling can be used to reduce the number of data points under the condition of the Nyquist sampling theorem. (The sampling rate or the Nyquist rate is equal to twice the upper cutoff frequency of a given signal.) To obtain reasonable data, the following four steps are used to process the data.

Dividing data into small bandwidth: during the mission time of the space-borne GW detectors, the evolution of DWD is expected to be small. Thus, the GW signals emitted from

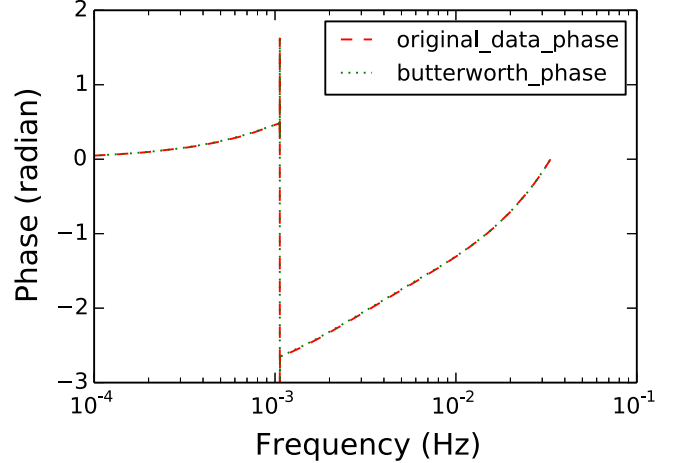


**Figure 1.** Comparison of signal phase before and after the Butterworth filtering. The frequency of the signal is 1.0627 mHz, and other parameters of the waveform are random. Here we adopt the Butterworth filter with bandpass of  $[f_1 - \epsilon, f_2 + \epsilon]$ , where  $\epsilon = 5 \times 10^{-6}$  Hz.

DWDs are nearly monochromatic. Therefore, one can split the MLDC-3.1 data into multiple frequency bands, each of which can be analyzed independently. The segment of each band chosen in this paper is 0.1 mHz. To reduce power leakage, the third-order Butterworth bandpass filter is adopted to obtain the narrowband data in the frequency band  $[f_1, f_2]$  ( $f_2 - f_1 = 0.1$  mHz) (Abbott et al. 2020). The Butterworth filter is applied twice, once forward and once backward. As shown in Figure 1, which is a comparison of the phase of the original data and that after the Butterworth filtering, the combined filter introduces zero phase shift.

In Figure 2, we plot the frequency response of the third-order Butterworth filter with passband  $[1.0, 1.1]$  mHz. One can see that the frequency response in the passband or the stop band is smooth without fluctuations, and the stop band attenuation gradually drops to zero. The filter can minimize the impact of the filter on the data as much as possible to preserve the integrity of the filtered data.

Frequency shift: The bandpassed data can be further downsampled if we heterodyne the data with a reference monochromatic wave  $q(t) = p(t)\cos(2\pi(f_1 - \epsilon)t)$ . A signal with original frequency of  $f_0$  will be shifted to lower frequency ( $f_0 - (f_1 - \epsilon)$ ) and higher frequency ( $f_0 + (f_1 - \epsilon)$ ) components. Here we have  $f_0 \in [f_1, f_2]$  and  $\epsilon$  is some small number. More details on the process can be found in Appendix D.

Lowpass filtering: We once again use Butterworth filtering for lowpass filtering  $[0, f_2 - f_1 + 2\epsilon]$  to filter out the high-frequency data. The lowpass filter frequency response is displayed in Figure 3. The Butterworth filter is applied twice: forward and backward in time.

Downsampling: After the above steps, the center frequency moves from  $f_0$  to  $(f_0 - (f_1 - \epsilon))$ , then we downsample the data

<sup>8</sup> The “bright” signals are the Galactic binaries in the MLDC-3.1 data set, whose SNR is greater than 10 in a single TDI-X channel (Babak et al. 2008b).

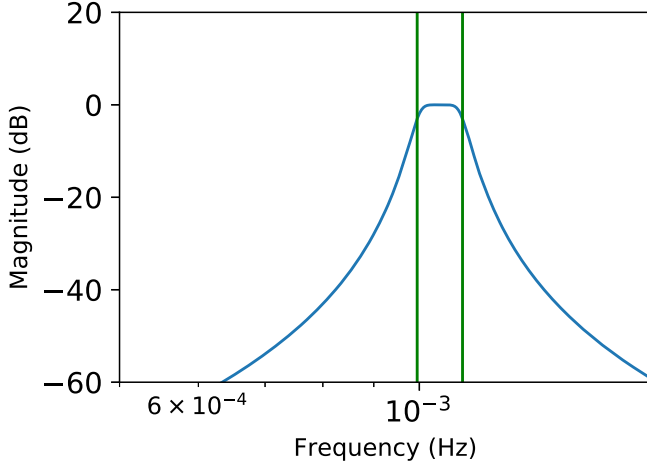


**Figure 2.** Frequency response of a third-order Butterworth filter for the frequency band of [1.0, 1.1] mHz.

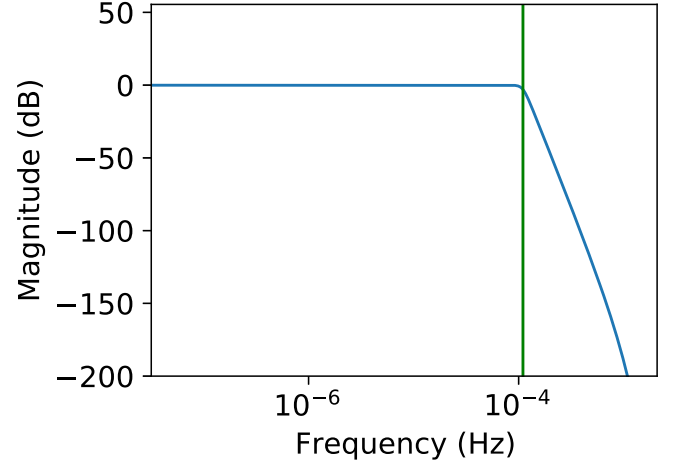


**Figure 3.** Frequency response of Butterworth filter for lowpass.

under the Nyquist sampling theorem and increase the sampling duration to reduce the amount of data.

The data processed through the above four steps are called DS-data. To test the downsampling method, we applied it to the MLDC-1.1.1a-blind data. In Figure 4, the top (bottom) panel shows the data of MLDC-1.1.1a-blind (noise-free signal) applying the downsampling method described above. In the figure, the red line is the original data; the blue line is the data after bandpass filtering, where the bandpass is  $[1 \text{ mHz} - \epsilon, 1.1 \text{ mHz} + \epsilon]$ , and one can find that the peak of the blue line is coincident with the original data; the yellow line is the data after frequency shift, and one can find that two peaks appear at high and low frequencies, respectively; the black line is the data after Butterworth lowpass filtering, and the peak at high frequency is filtered out; the green line is the data after downsampling. After the four steps, the number of data points has been reduced by a factor of around  $m_d \sim 300$  compared to the original data.

### 3.2. Generate Undersampled Waveform Template

To match the frequencies and number of data points in DS-data, the waveform templates should be processed in the same way as the DS-data. However, applying exactly the same procedures increases computational burden. The ideal scenario would be process DS-data once, and match with templates generated by downsampling. This aim can be achieved through undersampled waveform generation.

Undersampling is a technique that samples a bandpass filtered signal at a sampling rate lower than the Nyquist rate, but is still able to reconstruct the signal (Kester 2003). However, the undersample method may cause aliasing error (Bracewell 1986; Kester 2003). To fully reproduce the original signal, the undersampling rate needs to satisfy the following conditions: let  $f'_s = f_s/m_u$  be the undersampling rate; if

$\frac{2f_1}{n} \leq f'_s \leq \frac{2f_2}{n-1}$ , where integer  $n \in (1, \frac{f_2}{f_2-f_1}]$ ,  $f_s$  is the original sampling rate and  $m_u$  is a positive integer, then the original signal can be fully reproduced in  $[0, f'_s/2]$ . Also, a frequency shift like in the previous subsection is used to shift the waveform template to the location of the DS-data.

The data points of the templates obtained after undersampling should be the same as the data points of the data sets that have been downsampled. Then, the total number of points is reduced by a factor of  $m = \min[m_d, m_u]$ . The reduced number of data points can be different in different frequency bands. In Figure 5, a comparison is made between the data set after downsampling (i.e., DS-data) and the waveform template generated with undersampling. To quantify the difference between two signals, one can define the correlation or fitting factor (FF)

$$\text{FF} = \frac{(h_1|h_2)}{\sqrt{(h_1|h_1)}\sqrt{(h_2|h_2)}}. \quad (31)$$

After some calculation, we find that a typical signal would have  $\text{FF} \simeq 0.99996$  between the DS-data and the waveform generated with undersampling.

## 4. Search Method

Using the methods introduced in the previous section, now we have a DS-data set. In this section, we describe the construction of template banks. The search strategy is separated into two parts: (1) coarse search, in which we adopt a stochastic template bank method to quickly identify the signal candidates; (2) fine search, in which we use a PSO algorithm to explore small volumes in parameter space to determine the parameters of the signals.

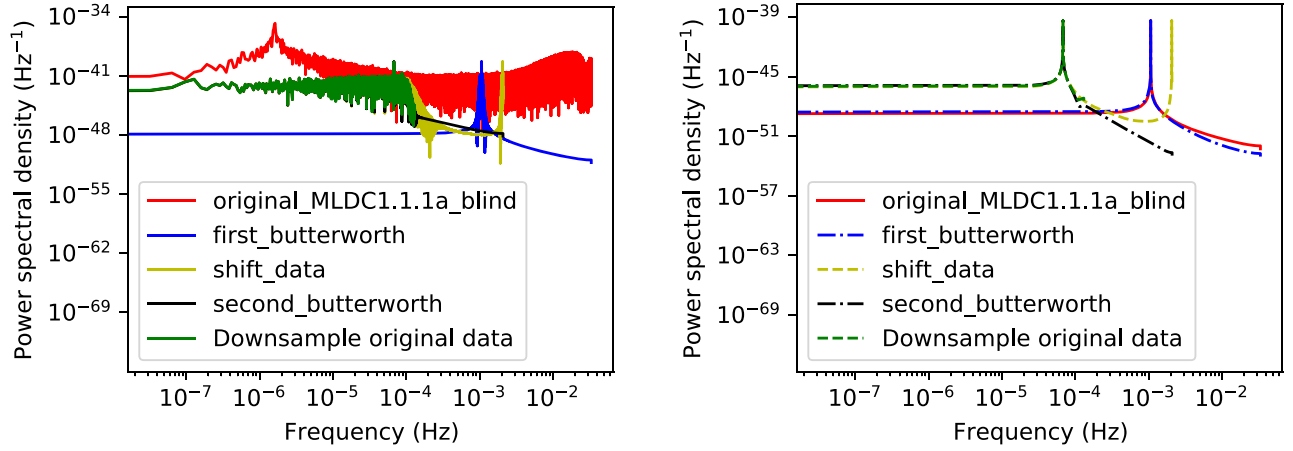


**Figure 4.** The left panel is the relationship between the frequency and PSD of the original data of MLDC1.1.1a-blind (there is only one signal in the data) and the original data after downsampling. The right is the same as the upper picture except that the data are noise-free.

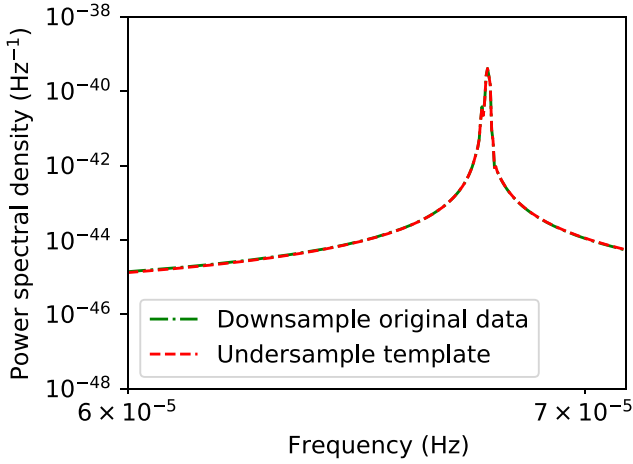


**Figure 5.** Comparison of the power spectra of the signal downsampling and template undersampling.

#### 4.1. Coarse Search

To generate the sample data points of the waveform, we need to specify model parameters. In the present paper, we will choose the template bank search method, thus a target template bank with model parameters needs to be built first. The template bank construction methods include regular lattice template banks, stochastic banks and random template banks. The latter two are expected to have less coverage than the regular one (Harry et al. 2009; Messenger et al. 2009). For the “random template bank,” the templates are placed randomly with probability distribution determined by the metric. The “stochastic template bank” is similar to the “random template bank” but with some additional pruning steps.

The implementation of the random template bank method is very simple, and can achieve surprisingly high levels of

efficiency compared to traditional template banks, especially at higher dimensions (Messenger et al. 2009; Allen 2022). For a given number of templates, compared with the random template bank method, the stochastic template bank will provide better coverage (Harry et al. 2009). The stochastic template bank is based on the “random template bank,” but subtracts those templates that are too close, or performs some other operations (for example, adjusting the position according to certain rules) (Babak 2008; Harry et al. 2009; Van Den Broeck et al. 2009; Fehrmann & Pletsch 2014; Harry et al. 2016; Indik et al. 2017; Allen 2021).

In this work, we choose the stochastic template bank approach proposed by Messenger et al. (2009). Nearly 100% parameter space coverage is achieved by subtracting templates that are too close together and then randomly populating some templates, iteratively. The method can be divided into the following three steps:

1. *Randomly generating templates in the parameter space*  $\mathcal{S}_n$ . If the coverage of the templates reaches  $\eta$  ( $\eta \in [0, 1)$ ) and the mismatch is  $m_*$ , the number of random templates we need will be  $N_R$  (Messenger et al. 2009)

$$N_R(\eta, m_*, \mathcal{S}_n) \approx \frac{V_{\mathcal{S}_n}}{V_n} \ln \left( \frac{1}{1 - \eta} \right) m_*^{-n/2}, \quad (32)$$

where  $V_n$  is the volume enclosed by an  $n$ -dimensional unit sphere, and the proper volume of the parameter space is  $V_{\mathcal{S}_n}$ .

2. *Removing templates that are too close together.* The distance between two templates at small separation is

$$d^2 = g_{ij} \Delta \Theta^i \Delta \Theta^j, \quad (33)$$

where  $g_{ij}$  is the metric of the parameter space. Calculate the distance  $d_{ij}$  between any two template points, and when  $d_{ij}$  is less than  $\sqrt{m_*}$ , remove one of them.



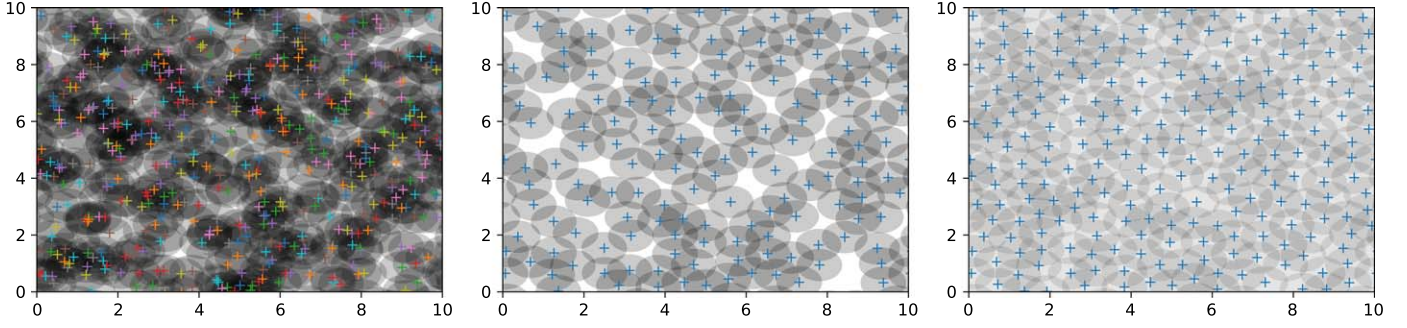


**Figure 6.** Schematic diagram of stochastic template bank generation in a two-dimensional parameter space, in which the initial coverage is  $\eta = 0.99$  and the mismatch criterion is  $m_* = 0.3$ .

Considering that the parameter space is curved, many issues will become complicated, e.g., the distance between widely separated points can no longer be easily computed and the determinant of the metric may be non-constant (Harry et al. 2009). There are also some efficient stochastic template methods (Manca & Vallisneri 2010; Fehrmann & Pletsch 2014). Since the efficiency is not dramatically different and here we focus on the implementation of the end-to-end data processing pipeline construction, we stick with the simpler realization of assuming that the metric  $g_{ij}$  of two points close to each other is flat (interested readers are referred to appendix A of Błaut et al. (2010) for more details).

3. Use step 1 to randomly generate about  $N_R$  new templates and inject them into the template bank obtained in step 2. Then, use step 2 to remove templates that are too close together. Repeat the above steps until the total number of templates no longer changes (Harry et al. 2009). At this time, the coverage of the template bank will be close to 100%.

To speed up the calculation of distances between every two templates in the template bank, in our study, the `KDTree` algorithm is utilized to speed up the calculation of the distance between templates in steps 2 and 3. An illustration of our entire calculation process of a simple example with two-dimensional parameter space is illustrated in Figure 6. In this paper, we have set the initial coverage as  $\eta = 0.99$  and the mismatch  $m_* = 0.3$ . Using the Monte Carlo simulation method as in Messenger et al. (2009), we computed the spatial coverage in the cases of two-dimensional parameters and obtained a Gaussian distribution with a mean of  $\eta = 0.99$ . Following the above three steps, the final coverages only get better, which suggest that the stochastic method implemented in our work is helpful in improving the coverage.

As mentioned in Section 2.5, the FFT algorithm can accelerate the calculation while the frequency points of the template bank match the Fourier frequencies. Thus, the parameter points of  $f$  are picked at the Fourier frequencies,

and at any frequency point, using the stochastic bank method described above, one can obtain a sub-template bank corresponding to the three parameters, i.e.,  $\{\lambda, \beta, \dot{f}\}$ . Then, the total number of templates in the template bank for the  $i$ -th frequency bin will be

$$N_{\text{total}}^i = N_R^i N_{\text{FFT}}^i, \quad (34)$$

where  $N_R^i$  is the number of the sub-template banks, and  $N_{\text{FFT}}$  is the number of points for the FFT. Note that  $N_R^i$  cannot be calculated exactly by Equation (32), due to the fact that the number of templates removed and added to the template bank is not necessarily the same.

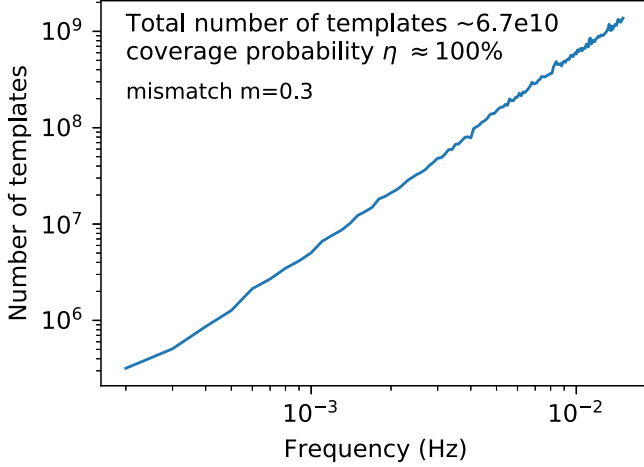
The target frequency band we search for in the MLDC-3.1 data is  $[1 \times 10^{-4}, 1.5 \times 10^{-2}]$  Hz, and we will separate this into 149 frequency bins. The number of signals above  $1.5 \times 10^{-2}$  Hz is very small and a complete search is not cost-effective. For the other parameters, we choose  $\beta \in [-\frac{\pi}{2}, \frac{\pi}{2}]$ ,  $\lambda \in [0, 2\pi]$  and  $\dot{f} \in [-3.8 \times 10^{-17}, 1.1 \times 10^{-15}]$  Hz<sup>2</sup> for  $f < 4$  mHz, and  $\dot{f} \in [-2.3 \times 10^{-14}, 7.7 \times 10^{-14}]$  Hz<sup>2</sup> for the rest.

Figure 7 plots the number of templates required for different frequency bands. The number of templates increases with frequency, and the total number of templates is about  $6 \times 10^{10}$ .

In the coarse search, we downsampled the original MLDC-3.1 data to get the DS-data, used the undersampling method to generate the waveform template and combined the FFT algorithm with stochastic template bank. The combination of these methods allows us to calculate the  $\mathcal{F}$ -statistic at a rate of about  $10^5 \sim 10^6$  per second. Adopting the coarse search, a 3.0 GHz core can search for the  $[1 \times 10^{-4}, 1.5 \times 10^{-2}]$  Hz signal within one day.

#### 4.2. Fine Search

After the coarse search, the large number of candidate signals obtained was clustered to eliminate redundancy. In order to refine the determination of match parameters, we adopt the fine search on top of the coarse search. In the fine search, one needs to find the maximum of the  $\mathcal{F}$ -statistic over the parameter space around the clustered templates.



**Figure 7.** Number of templates required for each frequency band. The total number of template banks for all frequency bands ( $[1 \times 10^{-4}, 1.5 \times 10^{-2}]$  Hz) is about  $6.7 \times 10^{10}$ .

Here we choose the PSO algorithm to do the fine search. The PSO algorithm is an evolutionary algorithm that relies on swarm dynamics to solve optimization problems. PSO algorithms have been utilized in astrophysics, such as pulsar timing (Taylor et al. 2012; Wang et al. 2014), ground-based GW astronomy (Wang & Mohanty 2010) and cosmic microwave background studies (Prasad & Souradeep 2012). This algorithm is particularly useful when trying to find the extrema of multimodal and nontrivial likelihood surfaces (Bouffanais & Porter 2016). Although there exist faster methods, we adopt the PSO method in the hope that this implementation can serve as a fiducial reference, where we can compare future quicker/smarter algorithms to assess their abilities.

#### 4.3. Pipeline

Figure 8 illustrates the entire search pipeline, including coarse search and fine search. The details are described as follows.

First, the coarse search method is adopted to search the TDI channels ( $X, Y, Z$ ), and the candidates with  $\mathcal{F}$  above the threshold  $\mathcal{F}_{th\_coarse}$  are kept, where we have chosen  $2\mathcal{F}_{th\_coarse} = \text{SNR}_{th\_coarse}^2 + 4 = 30$  corresponding to  $\text{SNR}_{th\_coarse} \simeq 5.1$ .

Second, the candidates that exceed the threshold at different frequency points are clustered together. It is important to note that due to the motion of the detector around the Sun, a Doppler shift will be included within the data. A real signal of frequency  $f_o$  from sources nearly everywhere on the sky will be broadened to the “double” Doppler window  $\pm 2 \times 10^{-4} f_o$  (Prix & Itoh 2005; Prix & Whelan 2007). The process is as follows:

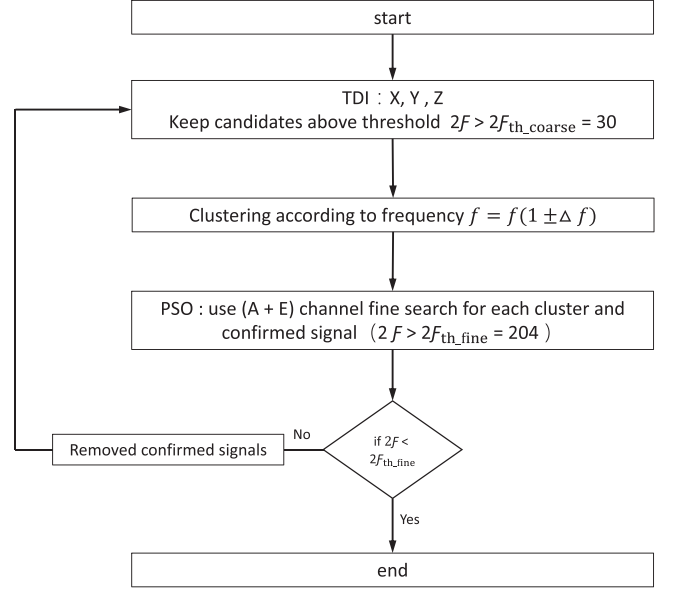


**Figure 8.** The pipeline we used.

1. Picking the one with the largest  $\mathcal{F}$ -statistic among all the candidates and the corresponding frequency is marked as  $f_c$ .
2. Finding the candidates whose frequency is between  $f_c - \Delta f$  and  $f_c + \Delta f$ , where  $\Delta f = 3 \times 10^{-4} f_c$  Hz.
3. Removing the candidates found in (2) and repeat the previous steps until all candidates have been screened.

Third, after clustering, the PSO<sup>9</sup> algorithm is used to do a “fine search” with the priori provided by each cluster on the DS-data. The TDI-A+E channel data are used in the fine search. The parameters are searched in the full range, except for the frequency which is based on the cluster size. In the fine search, we use the threshold  $2\mathcal{F}_{th\_fine} = 204$  or equivalently  $\text{SNR}_{th\_fine} \simeq 14.1$  (the SNR of the A+E channel is  $\sqrt{2}$  times higher than that of the single  $X, Y$  or  $Z$  channel). At the end of the fine search, we calculate the SNR with search parameters (considered foreground noise), and if the SNR of a single  $X$  channel is greater than 7, we accept the candidate. Note that the relationship between  $\mathcal{F}$ -statistic and SNR is not strict, see Equation (25).

Finally, the signal is reconstructed in time domain and removed from the data. Then, the previous steps are repeated until there is no more signal whose  $\mathcal{F}$ -statistic is greater than  $\mathcal{F}_{th\_fine}$ .

## 5. Results and Discussions

Using the pipeline mentioned above, from the MLDC-3.1 blind data set, we have detected 11,519 signals. In order to remove the false alarms, we adopt the following rule:

<sup>9</sup> We use the `scikit-opt` library.

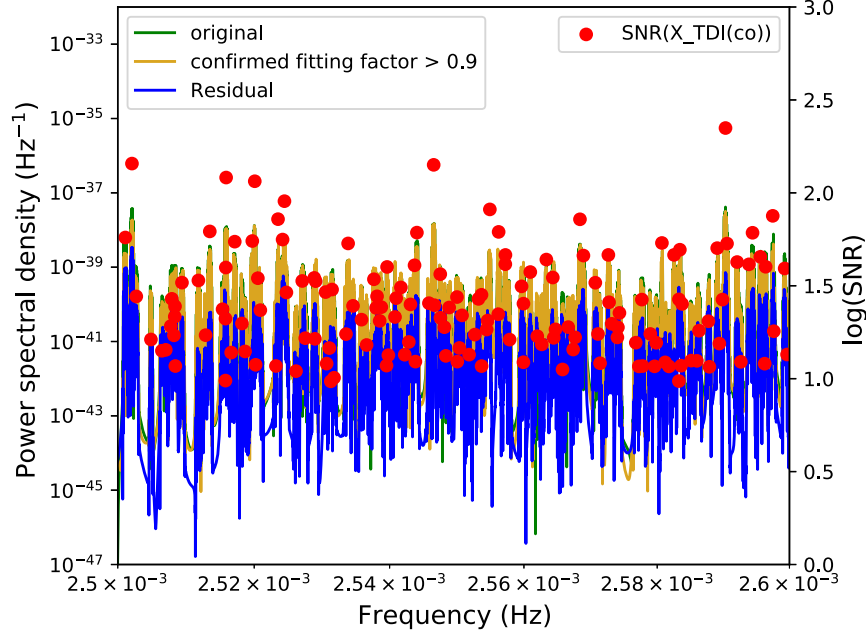


**Figure 9.** PSDs for the confirmed signals, the MLDC-3.1 real signals and the reduced data (removing signals) in the range of the [2.5, 2.6] mHz band. Solid red dots represent the SNR of the confirmed signals.

For two detected signals  $h_1$  and  $h_2$  with frequencies of  $f_1$  and  $f_2$  respectively, if  $f_1 - f_2 < 1/T_0 = \Delta f$  and the FF between the two signals is  $\geq 0.99$ , the two signals are considered to be the same, and only the signal with the larger  $\mathcal{F}$  is kept.

Applying the above criteria, 10,092 signals from 11,521 detected signals were confirmed.

### 5.1. Detection of Signals in a Single Band

We first describe the search in a typical frequency band between [2.5, 2.6] mHz. There are a total of 2342 bright sources in this frequency band in the MLDC-3.1 data set. We artificially stop the search when  $2\mathcal{F}_{\text{th\_fine}} = 204$  in the fine search process. In this frequency band, we detected 266 signals, and finally confirmed 209 signals. Each confirmed signal was paired with all the key signals (40 628 bright Galactic binaries that were injected in MLDC3.1) to verify. We only keep the maximum corresponding to FF for each confirmed signal. Among all the confirmed signals, there are 156 signals with  $\text{FF} \geq 0.9$ , 28 signals with  $0.8 \leq \text{FF} < 0.9$ , and 25 signals with  $\text{FF} < 0.8$ .

Figure 9 shows the spectrum of the detected signals and the real signals injected in the MLDC-3.1 data set. One may note that the residuals of the signals are very large. Continuing the search in this frequency band until there are no detection statistics having  $2\mathcal{F} > 102$  ( $\text{SNR} = 7$  corresponding to  $X$  channel), we detected 357 additional signals. Among these 357 signals, there are 246 signals with  $\text{FF} < 0.9$ . This suggests that the residuals are dominated by false signals. The ratio of the

real signal to the false signal is approximately 1:2. This indicates that the signal residuals can have a great impact on the detection of other signals, especially in the low-frequency bands where the signal density is high. A better way to cope with the effect of residuals may be using the global-fitting method, e.g., Littenberg et al. (2020).

### 5.2. Performance of the Search Method

Using Equation (31), the correlations of the confirmed signals with the injected signals in MLDC-3.1 blind data set are depicted in Figure 10. In all the confirmed signals, there are 8600 signals with FF greater than 0.9 and 1492 signals with FF less than 0.9. Among them, there are 573 signals whose FFs are greater than 0.8 while less than 0.9, and 107 signals whose FFs are greater than 0.7 while less than 0.8. From Figure 10, one can also find that there is an excess of candidates having correlations  $\text{FF} \sim 0$ . Moreover, most of the low FFs originate from the low frequencies, which is consistent with Błaut et al. (2010).

As described in Błaut et al. (2010), the excess of  $\text{FF} \sim 0$  signals may be caused by: (1) the imprecise parameter estimates for some low SNR signals; (2) many signals with low SNRs interfere with each other causing biases in the parameter estimation. Figure 11 shows the relationship between the frequency of all the confirmed signals and the corresponding SNRs. The color represents the value of the correlated FF; note that these FFs are calculated between our confirmed signals and the released keys of the MLDC-3.1 data set. In the

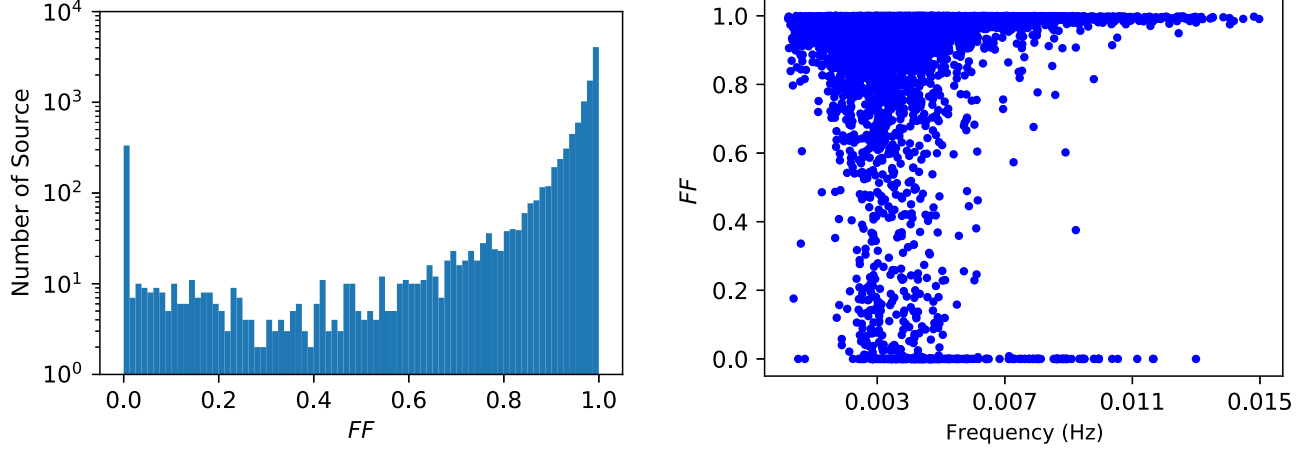


**Figure 10.** (Left) Histogram of the correlations between our confirmed signals and the injected signals of the MLDC-3.1 blind data set. (Right) Histogram of the correlations with respect to frequency.

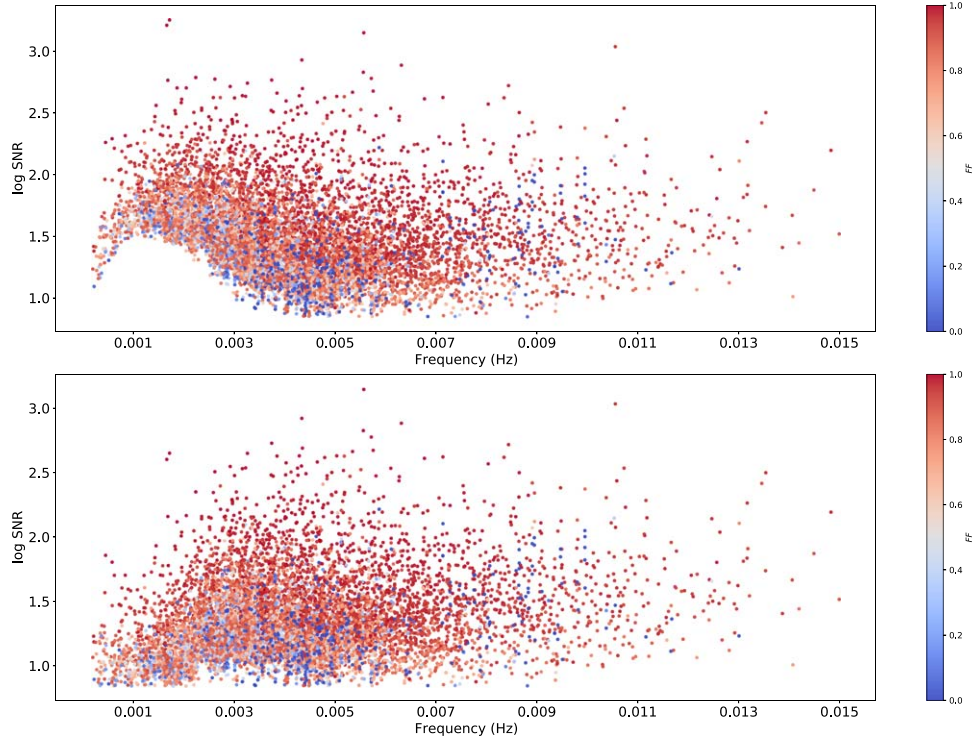


**Figure 11.** Relationship between the frequency of the confirmed signals and the SNR (top panel: no Galactic confusion noise; bottom panel: with Galactic confusion noise). The color of the dots represents the size of FF.

figure, most blue points are located at low SNRs, i.e., the signals with smaller FFs have mostly smaller SNRs, which indicate that the parameter estimation of signals with low SNRs will be poorer.

One can find that in the low frequency range at about  $1 \sim 3$  mHz, there is a blank area in the upper panel, which suggests that in this low frequency region, even some signals with large

SNRs may not be detected. This is mainly due to the fact that the SNRs displayed in the upper panel of Figure 11 are calculated without the Galactic confusion noise. When the Galactic confusion noise is taken into consideration, the block will disappear, just as shown in the bottom panel of Figure 11. This indicates that the Galactic confusion noise has a big influence on the detection of the GW signals from DWDs, and



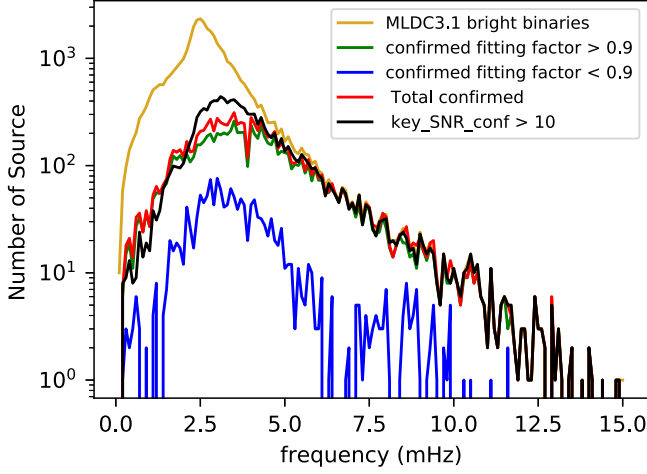


**Figure 12.** The number of confirmed signals by our search method and the number of signals in MLDC-3.1 bright binaries.

this also indicates that at the low frequency bands, the SNRs of the signals will be reduced due to the presence of Galactic confusion noise.

To verify this conclusion, the number of bright binaries of MLDC-3.1 and the confirmed signals of this paper in different frequency bands are plotted in Figure 12. One can find that the peak value of the bright signals and detection number is not in the same frequency band. The frequency band of the peak value of the detection number is higher. There are thousands of signals in each small frequency band around  $2.6 \times 10^{-3}$  Hz, where only hundreds of signals are confirmed. This suggests that a large number of signals at low frequencies can interfere with each other and become indistinguishable. Combining with Figure 11, one can see that these unresolvable bright signals form the Galactic confusion noise or foreground noise.

Meanwhile, the black line shown in Figure 12 is the number of the injected signals whose  $\text{SNR} > 10$  in the MLDC-3.1 data set (here, the Galactic foreground noise has been considered). One can find that the tendency of this line is similar with our confirmed signals, especially at high frequency and low frequency, which indicates that our method is trustworthy. The largest deviation appears around  $f \sim 3$  mHz, suggesting that the removal of a large number of signals will leave large residuals and have great impacts on the detection of the remaining signals.

Due to the presence of the foreground, the small SNRs prevent us from deepening the search sensitivity, and the increasing fraction of false alarms makes further search meaningless. At high frequencies, the aliasing of signals is significantly reduced, and the detection results gradually improve.

### 5.3. Performance of Parameter Estimation

Any systematic biases in the parameter estimation can be revealed by displaying the distribution of errors for all the confirmed signals (Littenberg 2011). We define the parameter errors and the fractional parameter error as (Babak et al. 2008b)

$$\Delta\lambda = \lambda_{\text{rec}} - \lambda_{\text{key}}, \quad (35)$$

$$\Delta\lambda/\lambda = (\lambda_{\text{rec}} - \lambda_{\text{key}})/\lambda_{\text{key}}, \quad (36)$$

where  $\lambda_{\text{rec}}$  is the parameter of the confirmed signals, and  $\lambda_{\text{key}}$  is the parameter of the injected signals of the MLDC-3.1 blind data. Histograms in Figure 13 depict the distribution of errors for all the signals we confirmed. Most of the frequency errors are within a small fraction of a Fourier bin ( $\Delta f = 1/T_0$ ), while the errors in frequency derivative are within  $\Delta f^2$ , and the errors in sky position are within  $\pm 0.05$  radians. In addition, the distributions of all the parameters have a strong peak at zero bias, which indicates that our results are reasonable.

### 5.4. Residuals

The ability of the signal search can be reflected in another way by comparing the remaining residuals with the noise. In Figure 14 we compared the smoothed spectrum of the MLDC-3.1 data set with that of data with confirmed signals removed. The two smoothed PSDs are compared with the PSD of the LISA instrumental noise (yellow line) and the analytical PSD of instrumental noise with the Galactic confusion noise (green line). Similar to the results shown in Blaut et al. (2010), one can also conclude that above the frequency of about 6 mHz, all the DWD systems are resolved well.

Another noteworthy issue is that we use an analytical PSD of instrumental noise plus the analytical PSD of Galactic confusion noise (i.e., Equation (B.1)) as the total PSD of noise when searching for a signal. As affirmed in Figure 14, in the low frequency bands, the convex part of the analytical total noise PSD matched well with the remaining residuals. This is good evidence that our search method performs well for searching signals in low frequencies.

In Figure 14, one may note that in the frequency bands around 0.0135 Hz and 0.0105 Hz, the residuals have some high peaks compared with the noise, which indicate that the detection capacity is poor in these frequency bands. To figure out why the residuals are still high, the injected signals' parameters are used to generate the waveform applying the analytical mathematical formula (i.e., Equation (1)–(4)), and then they are subtracted from the original data. The results are shown in Figure 15. One can find that the residuals are still higher than noise, thus the search method is still trustworthy.

## 6. Conclusions

The detection of galaxy DWDs can recover a large amount of information about the galaxy and remove a large amount of

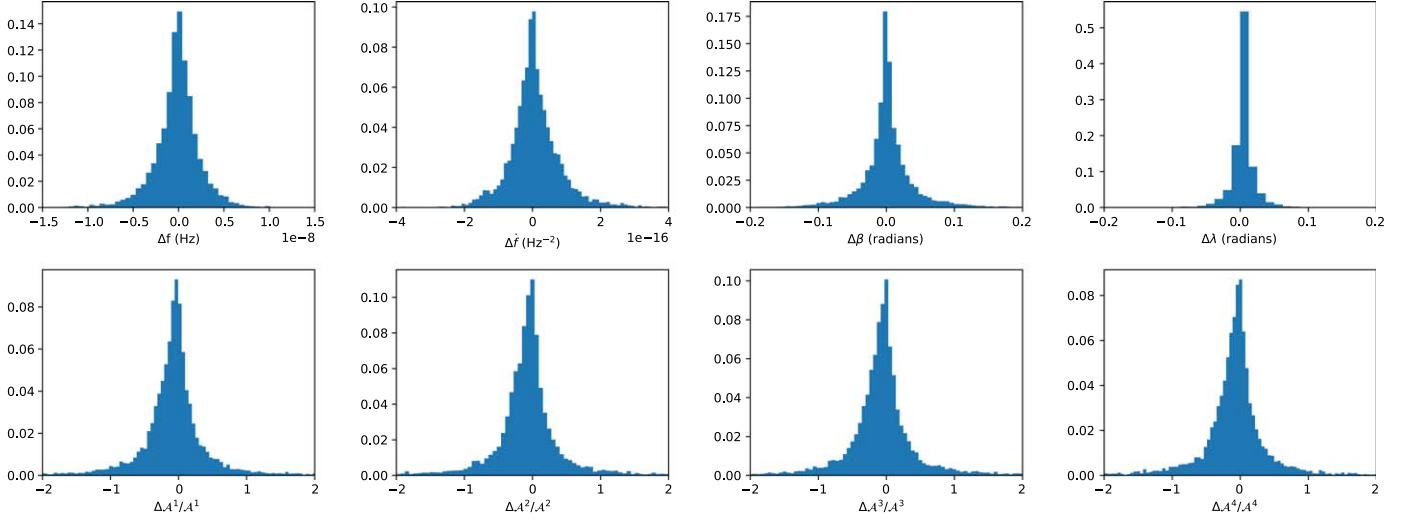


**Figure 13.** The error distribution between the source parameters we confirmed and the true source parameters in the MLDC-3.1 data set.

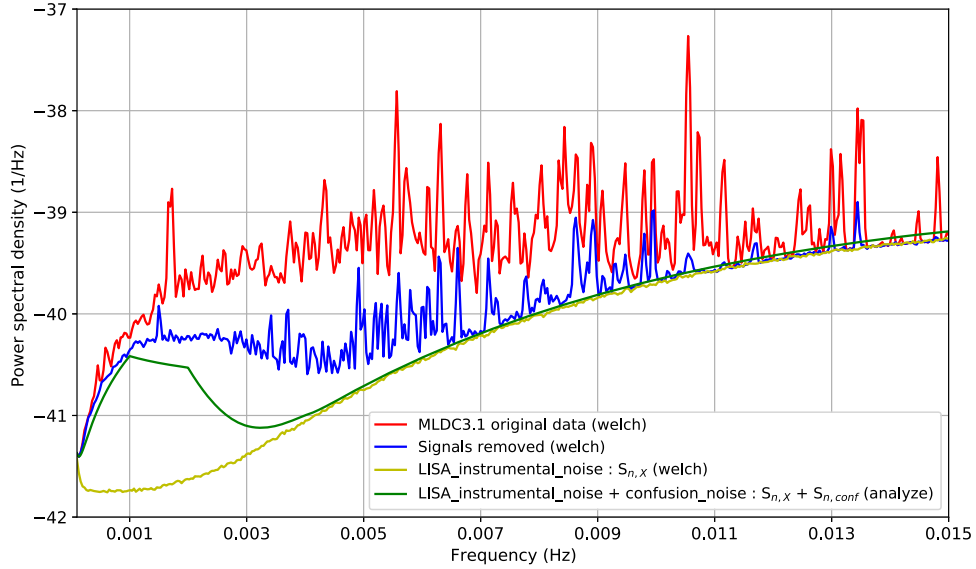


**Figure 14.** The red line is the smoothed PSD for the original MLDC-3.1 data, the blue line is that of reduced data after removing all confirmed signals, the yellow line is that of the LISA instrumental noise and the green one is the analytical total noise PSD.

foreground signal power to facilitate the search for signals at cosmological distances, such as the GWs of massive black hole binaries at high redshifts. However, the detection of DWDs faces enormous challenges: (1) how to effectively confirm signals in a huge number of DWDs ( $\sim 10^8$ ); (2) how to reduce calculation time while ensuring detection accuracy and quantity.

To solve these two problems, in this paper, we implement the detection process in two steps. The first step is the coarse search, in which we use the matched filtering method to match the data with the stochastic template bank, and can give a rough

estimation of the signals' parameters. The second step is the fine search, in which we adopt the PSO algorithm to accurately confirm the signal parameters, using the results of the coarse search as a priori.

For coverage of the template bank, we initially set it as  $\eta = 0.99$ , and this had been demonstrated by a Monte Carlo simulation method. By removing templates that are too close together and continuing to populate templates randomly until they could no longer be populated, our template bank coverage ends up approaching 100%. In this way, the area not covered by the template can be reduced to a minimum, e.g., Figure 6.

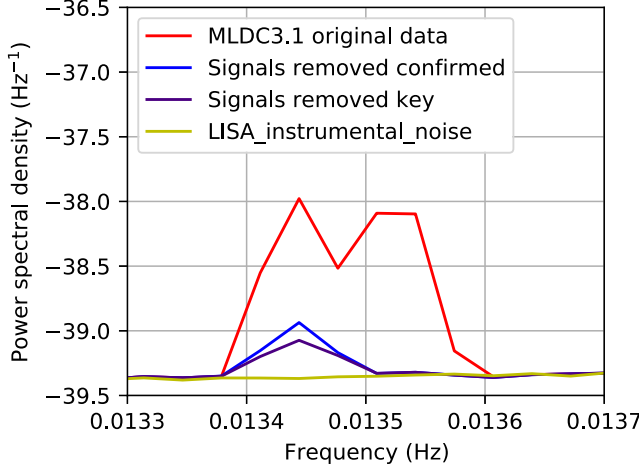


Figure 15. PSDs for different cases.

In order to speed up the calculation in coarse search, we downsampled the data set, undersampled the template and adopted the FFT algorithm in calculating the  $\mathcal{F}$ -statistic. The combination of these methods allows us to calculate the waveform template at about  $10^5 \sim 10^6$  per second, and the calculation of the whole frequency band with a normal core can be done within 24 hr. After the coarse search, the results of the coarse search are clustered, and then PSO algorithm is used to perform an accurate search within each cluster. Finally, we confirm 10,092 signals, and 8600 signals with FF greater than 0.9. The order of magnitude of our detected number of sources is consistent with previous studies (Babak et al. 2008a; Blaut et al. 2010; Littenberg 2011; Zhang et al. 2021), though a different detection method was adopted.

By analyzing the SNRs and PSD of the confirmed signals, error distribution of source parameters and PSD of residuals, we find that the Galactic confusion noise has a great influence on the detection of DWDs, especially at low frequencies. Our analysis also suggests that our method performs well in searching for signals in all frequency bands.

Last but not least, we used a PSO algorithm in the fine search stage. The search results serve well as a reference, but in terms of efficiency it is not the most efficient search algorithm. We aim to implement a more efficient search algorithm in the fine search stage and build the DWD analysis pipeline for TianQin based on this work in the future.

### Acknowledgments

This work has been supported by the Guangdong Major Project of Basic and Applied Basic Research (Grant No. 2019B030302001), the National Natural Science Foundation of China (NSFC, Grant No. 12173104), the fellowship of China Postdoctoral Science Foundation (Grant No. 2021M703769) and the Natural Science Foundation of Guangdong Province of

China (Grant No. 2022A1515011862). We acknowledge the support by National Supercomputer Center in Guangzhou.

## Appendix A Some Parameters of the Instrument

For LISA, the PSDs of the proof-mass noise and the optical-path noise are (Vallisneri 2005)

$$S^{\text{acc}} = 2.5 \times 10^{-48} \left( \frac{f}{1\text{Hz}} \right)^{-2} \left[ 1 + \left( \frac{10^{-4}\text{Hz}}{f} \right)^2 \right] \text{Hz}^{-1},$$

$$S^{\text{opt}} = 1.8 \times 10^{-37} \left( \frac{f}{1\text{Hz}} \right)^2 \text{Hz}^{-1}. \quad (\text{A1})$$

The arm-length of LISA is  $L = 2.5 \times 10^6$  km (Amaro-Seoane et al. 2017), but one should note that the arm-length that was used to generate MLDC-3.1 data is  $L = 5 \times 10^6$  km.

## Appendix B The Galactic Confusion Noise

MLDC-3.1 data contain a Galactic GW confusion from  $\sim 60$  million compact binary systems (Babak et al. 2008b). When we analyze MLDC-3.1 data we must add an estimate of the confusion noise  $S_{n,\text{conf}}(f)$  which is derived from data simulations (Timpano et al. 2006):

$$S_{n,\text{conf}}(f) = 16(2\pi f L)^2 \sin^2(2\pi f L) \text{Hz}^{-1}$$

$$\times \begin{cases} 10^{-44.62}(f/\text{Hz})^{-2.3}, & f \in [10^{-4}, 10^{-3}]\text{Hz}, \\ 10^{-50.92}(f/\text{Hz})^{-4.4}, & f \in [10^{-3}, 10^{-2.7}]\text{Hz}, \\ 10^{-62.8}(f/\text{Hz})^{-8.8}, & f \in [10^{-2.7}, 10^{-2.4}]\text{Hz}, \\ 10^{-89.68}(f/\text{Hz})^{-20.0}, & f \in [10^{-2.4}, 10^{-2.0}]\text{Hz}. \end{cases} \quad (\text{B1})$$

## Appendix C Analytical Derivation of the Extrinsic Parameters

The  $\mathcal{F}$ -statistic depends only on  $\{\lambda, \beta, f, \dot{f}\}$ . Inverting the four relations  $\mathcal{A}^\mu(\phi_0, \psi, \iota, h_0)$  defined in Equation (9), one can obtain the extrinsic parameters analytically. First, we define two new parameters  $A_{\text{sum}}$  and  $D_a$  as

$$A_{\text{sum}} \equiv \sum_{\mu=1}^4 (\mathcal{A}^\mu)^2 = A_+^2 + A_\times^2. \quad (\text{C1})$$

$$D_a \equiv \mathcal{A}^1 \mathcal{A}^4 - \mathcal{A}^2 \mathcal{A}^3 = A_+ A_\times. \quad (\text{C2})$$

Using Equations (C1) and (C2), one has

$$2A_{+,\times}^2 = A_{\text{sum}} \pm \sqrt{A_{\text{sum}}^2 - 4D_a^2}. \quad (\text{C3})$$

As defined in Equations (1) and (2), one has  $|A_+| \geq |A_\times|$ , which means that the sign of  $A_+$  must be positive, while the

sign of  $A_{\times}$  is determined by the sign of  $D_a$ . Thus,

$$A_+ = \sqrt{(A_{\text{sum}} + \sqrt{A_{\text{sum}}^2 - 4D_a^2})/2}. \quad (\text{C4})$$

$$A_{\times} = \sqrt{(A_{\text{sum}} - \sqrt{A_{\text{sum}}^2 - 4D_a^2})/2}. \quad (\text{C5})$$

Combining the above equations, one can easily obtain

$$\psi = \frac{1}{2} \arctan \left( \frac{\mathcal{A}^4 A_+ - \mathcal{A}^4 A_{\times}}{\mathcal{A}^3 A_+ + \mathcal{A}^2 A_{\times}} \right). \quad (\text{C6})$$

$$\phi_0 = \arctan \left( \frac{\mathcal{A}^3 A_+ + \mathcal{A}^2 A_{\times}}{\mathcal{A}^4 A_{\times} - \mathcal{A}^4 A_+} \right). \quad (\text{C7})$$

$$h_0 = A_+ + \sqrt{A_+^2 - A_{\times}^2}. \quad (\text{C8})$$

$$\iota = \arccos \left( \frac{A_{\times}}{h_0} \right). \quad (\text{C9})$$

## Appendix D

### Principle of Data Frequency Mixing

The FT of the cosine function is

$$\cos(2\pi f_0 t) \xrightarrow{\text{FT}} \pi [\delta(f + f_0) + \delta(f - f_0)]. \quad (\text{D1})$$

Assuming that  $p(t)$  and  $q(t)$  are different time domain data, and both have FTs, namely  $\tilde{p}(f)$ ,  $\tilde{q}(f)$ , multiplying two data in the time domain is equal to their respective FT convolution, where “\*” means convolution,

$$p(t)q(t) \xrightarrow{\text{FT}} \frac{1}{2\pi} \tilde{p}(f) * \tilde{q}(f). \quad (\text{D2})$$

Let  $q(t) = p(t)\cos(2\pi f_0 t)$ , then according to Equations (D1) and (D2) we get

$$\begin{aligned} \tilde{q}(f) &= \frac{1}{2\pi} \tilde{p}(f) * \pi [\delta(f + f_0) + \delta(f - f_0)] \\ &= \frac{1}{2} [\tilde{p}(f + f_0) + \tilde{p}(f - f_0)]. \end{aligned} \quad (\text{D3})$$

Thus, one can find that we can get two peaks after the data are shifted.

## ORCID iDs

Yang Lu (卢杨)  <https://orcid.org/0000-0002-0595-8918>  
En-Kun Li (李恩坤)  <https://orcid.org/0000-0002-3186-8721>  
Yi-Ming Hu (胡一鸣)  <https://orcid.org/0000-0002-7869-0174>  
Jian-dong Zhang (张建东)  <https://orcid.org/0000-0002-5930-6739>

## References

Aasi, J., Abadie, J., Abbott, B. P., et al. 2015, *CQGra*, 32, 074001  
Abbott, B. P., Abbott, R., Abbott, T. D., et al. 2016, *PhRvL*, 116, 061102

- Abbott, B. P., Abbott, R., & Abbott, T. D. 2019, *PhRvX*, 9, 031040  
Abbott, B. P., Abbott, R., Abbott, T. D., et al. 2020, *CQGra*, 37, 055002  
Abbott, B., Abbott, R., Adhikari, R., et al. 2004, *PhRvD*, 69, 082004  
Abbott, B., Abbott, R., Adhikari, R., et al. 2007, *PhRvD*, 76, 082001  
Abbott, R., Abbott, T. D., Abraham, S., et al. 2021a, *PhRvX*, 11, 021053  
Abbott, R., Abbott, T. D., Acernese, F., et al. 2021b, arXiv:2108.01045  
Abbott, R., Abbott, T. D., Acernese, F., et al. 2021c, arXiv:2111.03606  
Accadia, T., Acernese, F., Alshourbagy, M., et al. 2012, *JINST*, 7, P03012  
Acernese, F., Agathos, M., Agatsuma, K., et al. 2015, *CQGra*, 32, 024001  
Adams, M. R., Cornish, N. J., & Littenberg, T. B. 2012, *PhRvD*, 86, 124032  
Allen, B. 2021, *PhRvD*, 104, 042005  
Allen, B. 2022, *PhRvD*, 105, 102003  
Allen, B., Anderson, W. G., Brady, P. R., Brown, D. A., & Creighton, J. D. E. 2012, *PhRvD*, 85, 122006  
Amaro-Seoane, P., Audley, H., Babak, S., et al. 2017, arXiv:1702.00786  
Armstrong, J. W., Estabrook, F. B., & Tinto, M. 1999, *ApJ*, 527, 814  
Arnaud, K. A., Babak, S., Baker, J. G., et al. 2006, *AIP Conf. Proc.*, 873, 619  
Arnaud, K. A., Babak, S., Baker, J. G., et al. 2007a, *CQGra*, 24, S551  
Arnaud, K. A., Auger, G., Babak, S., et al. 2007b, *CQGra*, 24, S529  
Aso, Y., Michimura, Y., Somiya, K., et al. 2013, *PhRvD*, 88, 043007  
Astone, P., Borkowski, K. M., Jaranowski, P., Pietka, M., & Krolak, A. 2010, *PhRvD*, 82, 022005  
Babak, S. 2008, *CQGra*, 25, 195011  
Babak, S., Balasubramanian, R., Churches, D., Cokelaer, T., & Sathyaprakash, B. S. 2006, *CQGra*, 23, 5477  
Babak, S., Baker, J. G., Benacquista, M. J., et al. 2008a, *CQGra*, 25, 114037  
Babak, S., Baker, J. G., Benacquista, M. J., et al. 2008b, *CQGra*, 25, 184026  
Babak, S., Baker, J. G., Benacquista, M. J., et al. 2010, *CQGra*, 27, 084009  
Barone-Nugent, R. L., Lidman, C., Wyithe, J. S. B., et al. 2012, *MNRAS*, 425, 1007  
Belczynski, K., Kalogera, V., & Bulik, T. 2002, *ApJ*, 572, 407  
Benacquista, M., & Holley-Bockelmann, K. 2006, *ApJ*, 645, 589  
Blaut, A., Babak, S., & Królak, A. 2010, *PhRvD*, 81, 063008  
Blaut, A., Krolak, A., & Babak, S. 2009, *CQGra*, 26, 204023  
Bouffanais, Y., & Porter, E. K. 2016, *PhRvD*, 93, 064020  
Bracewell, R. N. 1986, *The Fourier Transform and Its Applications* (3rd edn.; New York: McGraw-Hill)  
Breivik, K., Coughlin, S., Zevin, M., et al. 2020, *ApJ*, 898, 71  
Brown, D. A., Crowder, J., Cutler, C., Mandel, I., & Vallisneri, M. 2007, *CQGra*, 24, S595  
Calabrese, E., Hložek, R. A., Bond, J. R., et al. 2017, *PhRvD*, 95, 063525  
Cornish, N. J., & Crowder, J. 2005, *PhRvD*, 72, 043005  
Crowder, J., & Cornish, N. J. 2004, *PhRvD*, 70, 082004  
Crowder, J., & Cornish, N. J. 2007, *CQGra*, 24, S575  
Cutler, C., & Flanagan, E. E. 1994, *PhRvD*, 49, 2658  
Cutler, C., & Schutz, B. F. 2005, *PhRvD*, 72, 063006  
Dall’Osso, S., & Rossi, E. M. 2014, *MNRAS*, 443, 1057  
Estabrook, F. B., Tinto, M., & Armstrong, J. W. 2000, *PhRvD*, 62, 042002  
Fan, H.-M., Hu, Y.-M., Barausse, E., et al. 2020, *PhRvD*, 102, 063016  
Fehrmann, H., & Pletsch, H. J. 2014, *PhRvD*, 90, 124049  
Finn, L. S. 1992, *PhRvD*, 46, 5236  
Fuller, J., & Lai, D. 2012, *ApJL*, 756, 17  
Hall, E. D., Cahillane, C., Izumi, K., Smith, R. J. E., & Adhikari, R. X. 2019, *CQGra*, 36, 205006  
Harry, I., Privitera, S., Bohé, A., & Buonanno, A. 2016, *PhRvD*, 94, 024012  
Harry, I. W., Allen, B., & Sathyaprakash, B. S. 2009, *PhRvD*, 80, 104014  
Helström, C. 1968, *International Series of Monographs in Electronics and Instrumentation, Statistical Theory of Signal Detection*, Vol. 9 (New York: Pergamon)  
Huang, S.-J., Hu, Y.-M., Korol, V., et al. 2020, *PhRvD*, 102, 063021  
Indik, N., Haris, K., Dal Canton, T., et al. 2017, *PhRvD*, 95, 064056  
Jaranowski, P., & Krolak, A. 2005, *LRR*, 8, 3  
Jaranowski, P., Krolak, A., & Schutz, B. F. 1998, *PhRvD*, 58, 063001  
John C., & Neil J. A. Sloane 1999, *Sphere Packings, Lattices and Groups* (3rd edn.; New York: Springer)  
Katz, M. L., Kelley, L. Z., Dosopoulou, F., et al. 2020, *MNRAS*, 491, 2301  
Kester, W. 2003, *Mixed-signal and DSP design techniques* (Oxford and Boston: Newnes)  
Korol, V., Rossi, E. M., & Barausse, E. 2019, *MNRAS*, 483, 5518



- Krolak, A., Tinto, M., & Vallisneri, M. 2004, *PhRvD*, **70**, 022003 [Erratum: Phys.Rev.D 76, 069 901 (2007)]
- Kyutoku, K., & Seto, N. 2016, *MNRAS*, **462**, 2177
- Lamberts, A., Garrison-Kimmel, S., Hopkins, P., et al. 2018, *MNRAS*, **480**, 2704
- LDC 2019, LISA Data Challenges, <https://lisa-ldc.lal.in2p3.fr>.
- Liang, Z.-C., Hu, Y.-M., Jiang, Y., et al. 2022, *PhRvD*, **105**, 022001
- Littenberg, T. B. 2011, *PhRvD*, **84**, 063009
- Littenberg, T., Cornish, N., Lackeos, K., & Robson, T. 2020, *PhRvD*, **101**, 123021
- Liu, S., Hu, Y.-M., Zhang, J.-d., & Mei, J. 2020, *PhRvD*, **101**, 103027
- Luo, J., Chen, L.-S., Duan, H.-Z., et al. 2016, *CQGra*, **33**, 035010
- Manca, G. M., & Vallisneri, M. 2010, *PhRvD*, **81**, 024004
- Marsh, T. R., Nelemans, G., & Steeghs, D. 2004, *MNRAS*, **350**, 113
- Messenger, C., Prix, R., & Papa, M. A. 2009, *PhRvD*, **79**, 104017
- MLDC 2006, Mock LISA Data Challenge, <https://astrogravs.nasa.gov/docs/mldc/>
- Nelemans, G., Yungelson, L. R., & Portegies Zwart, S. F. 2001a, *A&A*, **375**, 890
- Nelemans, G., Yungelson, L. R., Portegies Zwart, S. F., & Verbunt, F. 2001b, *A&A*, **365**, 491
- Perlmutter, S., Aldering, G., Goldhaber, G., et al. 1999, *ApJ*, **517**, 565
- Pisarski, A., & Jaranowski, P. 2015, *CQGra*, **32**, 145014
- Postnov, K. A., & Yungelson, L. R. 2014, *LRR*, **17**, 3
- Prasad, J., & Souradeep, T. 2012, *PhRvD*, **85**, 123008 [Erratum: Phys.Rev.D 90, 109 903 (2014)]
- Prince, T. A., Tinto, M., Larson, S. L., & Armstrong, J. W. 2002, *PhRvD*, **66**, 122002
- Prix, R. 2007, *PhRvD*, **75**, 023004 [Erratum: Phys.Rev.D 75, 069 901 (2007)]
- Prix, R., & Itoh, Y. 2005, *CQGra*, **22**, S1003
- Prix, R., & Whelan, J. T. 2007, *CQGra*, **24**, S565
- Riess, A. G., Filippenko, A. V., Challis, P., et al. 1998, *AJ*, **116**, 1009
- Romano, J. D., & Cornish, N. J. 2017, *LRR*, **20**, 2
- Sesana, A. 2016, *PhRvL*, **116**, 231102
- Solheim, J. E. 2010, *PASP*, **122**, 1133
- Somiya, K. 2012, *CQGra*, **29**, 124007
- Tauris, T. M. 2018, *PhRvL*, **121**, 131105 [Erratum: Phys.Rev.Lett. 124, 149 902 (2020)]
- Taylor, S. R., Gair, J. R., & Lentati, L. 2012, arXiv:1210.3489
- Timpano, S. E., Rubbo, L. J., & Cornish, N. J. 2006, *PhRvD*, **73**, 122001
- Vallisneri, M. 2005, *PhRvD*, **71**, 022001
- Van Den Broeck, C., Brown, D. A., Cokelaer, T., et al. 2009, *PhRvD*, **80**, 024009
- Wang, H.-T., Jiang, Z., Sesana, A., et al. 2019, *PhRvD*, **100**, 043003
- Wang, Y., & Mohanty, S. D. 2010, *PhRvD*, **81**, 063002
- Wang, Y., Mohanty, S. D., & Jenet, F. A. 2014, *ApJ*, **795**, 96
- Wette, K. 2014, *PhRvD*, **90**, 122010
- Wilhelm, M. J. C., Korol, V., Rossi, E. M., & D'Onghia, E. 2020, *MNRAS*, **500**, 4958
- Yu, S., & Jeffery, C. S. 2010, *A&A*, **521**, A85
- Zhang, X., Mohanty, S. D., Zou, X., & Liu, Y. 2021, *PhRvD*, **104**, 024023